

Enabling *P*-type Conduction in Bilayer WS₂ with NbP Topological Semimetal Contacts

Lauren Hoang^{1,#}, Asir Intisar Khan^{1,#}, Robert K.A. Bennett¹, Hyun-mi Kim², Zhepeng Zhang³, Marisa Hocking³, Ae Rim Choi⁴, Il-Kwon Oh⁴, Andrew J. Mannix^{3,5*}, and Eric Pop^{1,3,6,7*}

¹*Department of Electrical Engineering, Stanford University, Stanford, CA 94305, USA*

²*Korea Electronics Technology Institute, Seongnam-si 13509, Republic of Korea*

³*Department of Materials Science & Engineering, Stanford University, Stanford, CA 94305, USA*

⁴*Department of Intelligence Semiconductor Engineering, Ajou University, Suwon 16499, Republic of Korea*

⁵*Stanford Institute for Materials & Energy Sciences, SLAC National Accelerator Lab., Menlo Park, CA 94025, USA*

⁶*Department of Applied Physics, Stanford University, Stanford, CA 94305, USA*

⁷*Precourt Institute for Energy, Stanford University, Stanford, CA 94305, USA*

[#]*These authors contributed equally to this work.*

^{*}*E-mail: ajmannix@stanford.edu, epop@stanford.edu*

Two-dimensional (2D) semiconductors are promising for low-power complementary metal oxide semiconductor (CMOS) electronics, which require ultrathin *n*- and *p*-type transistor channels. Among 2D semiconductors, WS₂ is expected to have good conduction for both electrons and holes, but *p*-type WS₂ transistors have been difficult to realize due to the relatively ‘deep’ valence band and the presence of mid-gap states with conventional metal contacts. Here, we report topological semimetal NbP as *p*-type electrical contacts to bilayer WS₂ with up to 5.8 μA/μm hole current at room temperature; this is the highest to date for sub-2 nm thin WS₂ and > 50× larger than with metals like Ni or Pd. The *p*-type conduction is enabled by the simultaneously high work function and low density of states of the NbP, which reduce Fermi level pinning. These contacts are sputter-deposited at room temperature, an approach compatible with CMOS fabrication, a step towards enabling ultrathin WS₂ semiconductors in future nanoelectronics.

Computing in the 21st century must process increasingly complex data loads, with recent large language models estimated to use as much energy as a small city every day¹. From the hardware side, reducing energy use could be addressed by three-dimensional (3D) integration of logic and memory with dense interconnects, an approach that could yield 100× or higher energy efficiency per function². Dense 3D integration calls for materials stacked at sufficiently low temperatures to avoid damaging existing (memory or logic) layers^{3,4}, and low-power operation requires complementary metal oxide semiconductor (CMOS) technology, with both *n*- and *p*-type transistors^{5,6}. Energy-efficient, 3D electronics could benefit from adopting two-dimensional (2D) semiconductors, in nanosheet transistors⁷

or in back-end-of-line (BEOL) logic and memory layers, due to their favorable mobility in sub-2 nm thin films^{8,9} and their compatibility with lower temperature fabrication^{10,11} than crystalline silicon.

Among 2D semiconductors, tungsten disulfide (WS_2) is one of the few expected to have simultaneously good electron and hole mobility⁹, allowing it to serve as a single material for both *n*- and *p*-type future transistors, unlike MoS_2 and WSe_2 . WS_2 also has one of the larger band gaps among 2D semiconductors (> 2.2 eV for bi- or monolayers)¹², an advantage for low power operation. However, its valence band is ‘deeper’, with respect to the vacuum level, than the Fermi level of most common metals with work function up to 5.6 eV; this is a key reason why *p*-type contacts have been difficult to achieve with WS_2 , compared to WSe_2 or other 2D materials having ‘shallower’ valence bands. Conventional metals may also cause metal- and defect-induced gap states (MIGS and DIGS) that pin the Fermi level unfavorably (**Fig. 1a**), and although this effect could be reduced with Bi or Sb for *n*-type devices¹³, the low work function of such semimetals limits their use for *p*-type contacts.

Here we achieve record *p*-type current in bilayer WS_2 (~1.3 nm thin) with NbP semimetal contacts. These semimetals are expected to have large work function based on recent density functional theory (DFT) calculations¹⁴, and their low density of states near the Fermi level could limit Fermi level pinning, enabling improved hole injection (**Fig. 1b**). NbP is also a Weyl semimetal, previously found to show signatures of topological protection in single crystal¹⁵ and ultrathin nanocrystalline films¹⁶ similar to Bi_2Se_3 ¹⁷. When interfaced with bilayer WS_2 , such topological semimetals could display suppressed MIGS, and their large work function better aligns the Fermi level with the bilayer WS_2 valence band (**Fig. 1b,c**, **Supplementary Fig. S1**), both desired features for *p*-type conduction.

Importantly, our NbP contacts were sputter-deposited directly onto WS_2 at room temperature, a process compatible with 3D integration and BEOL fabrication³ (see **Methods** for details). However, NbP contacts sputtered on *monolayer* WS_2 were found to cause some defects (see **Supplementary Fig. S2 and S3a**); thus, we focus primarily on *bilayer* WS_2 in this study, which has higher immunity to process damage (**Supplementary Fig. S3b**) and a higher valence band¹² than monolayer WS_2 .

To examine the interface of NbP contacts with bilayer WS_2 , we performed high-resolution scanning transmission electron microscopy (STEM) across such a stack on SiO_2/Si (**Fig. 2a-c**), similar to the transistor contacts employed further below. Here, the bilayer WS_2 films were directly grown by chemical vapor deposition (CVD)¹⁸ onto the SiO_2/Si substrate. STEM images show the conformal deposition of ~3.5 nm sputtered NbP onto bilayer WS_2 without obvious defects (**Fig. 2a**).

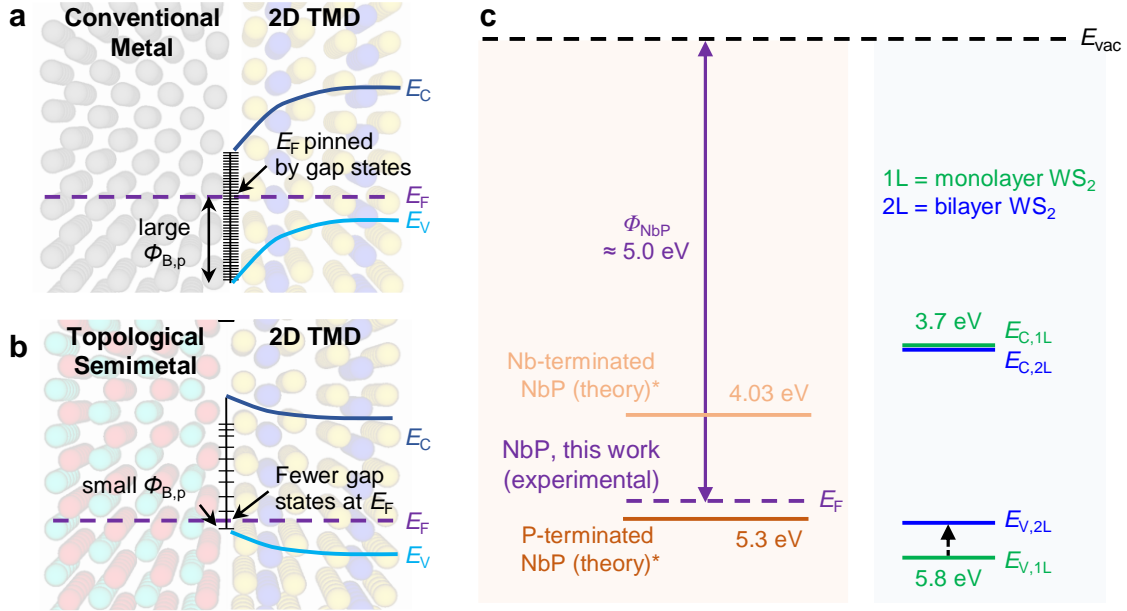


Figure 1 | Metal and topological semimetal NbP interfaces with WS₂. **a**, Conventional metal, and **b**, topological semimetal interfaced with a 2D semiconductor (here, WS₂). The conventional metal tends to cause significant Fermi level (E_F) pinning in the band gap, leading to large Schottky barrier height for hole conduction ($\phi_{B,p} = E_F - E_V$). In contrast, topological semimetals with large work functions, such as NbP (and TaP), are expected to have less pinning and lower hole barrier height. E_C and E_V denote the conduction and valence band edges, respectively. **c**, Schematic diagram of NbP–WS₂ band alignments. The valence band of bilayer (2L) WS₂ is higher than that of monolayer (1L), and better aligned with our experimental work function of NbP (see **Supplementary Fig. S1**). The expected work function of NbP (marked by *) and the WS₂ bands in the figure are based on Refs. 12, 14.

The elemental energy dispersive spectra (EDS) in **Fig. 2d-h** confirm uniform distribution of Nb and P in our NbP film on bilayer WS₂. Atomic force microscope (AFM) mapping also reveals low surface roughness and continuous NbP both on SiO₂ (**Supplementary Fig. S4a**) and WS₂ (**Fig. 2i** and **Supplementary Fig. S4b**). Previous work has found that many metals deposited on 2D semiconductor surfaces tend to aggregate and form clusters^{19,20}. However, our NbP deposited on WS₂ has no measurable change in surface roughness compared to when sputtered on SiO₂. Both top-down AFM and cross-sectional TEM imaging suggest intimate NbP-WS₂ contacts, without agglomeration. We also used Raman spectroscopy before and after NbP deposition, finding that the E_g and A_{1g} peaks of bilayer WS₂ (**Fig. 2j**) are essentially unaffected by the deposition of NbP (of either ~2 nm or ~3.5 nm thickness), unlike for monolayer WS₂ (**Supplementary Fig. S3a**). However, the formation of some defects is not unexpected^{20,21} after direct sputtering of NbP on WS₂, as suggested by the increased LA(M) peak intensity²² (**Supplementary Fig. S3b-d**), especially as the number of WS₂ layers is decreased.

We fabricated bilayer WS₂ transistors with NbP and TaP contacts (**Fig. 3a,b**), capped by Pd/Au, as well as control devices with only Pd/Au contacts. Devices have channel lengths L between 100 nm and 1 μ m, channel widths of 1 or 2 μ m, and are back-gated by the heavily doped Si substrate through

100 nm SiO₂. A top-down scanning electron microscope (SEM) image of a WS₂ bilayer ‘strip’ with multiple device channels is shown in **Fig. 3b**, and additional fabrication details are given in **Methods**.

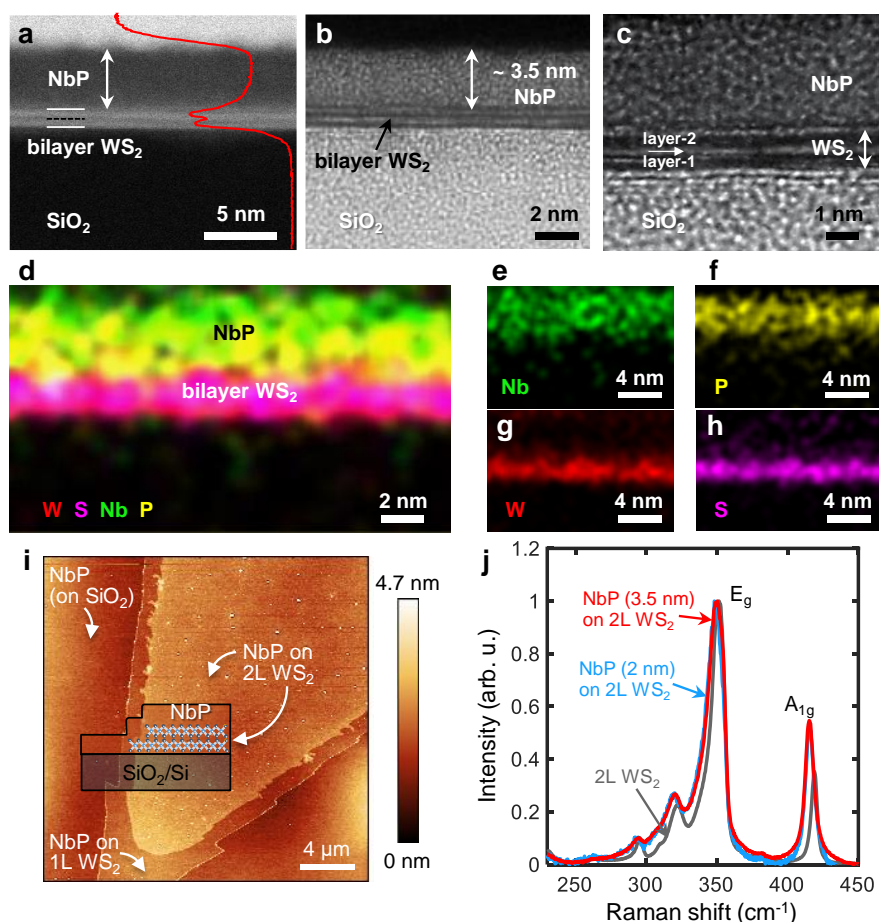


Figure 2 | Characterization of the NbP/bilayer WS₂ interface. **a**, High-angle annular dark field imaging (HAADF) scanning transmission electron microscopy (STEM) cross-section of NbP sputtered onto bilayer WS₂ on an SiO₂/Si substrate. STEM shows ~3.5 nm NbP film conformally deposited on the ~1.3 nm thin bilayer WS₂ (horizontal lines mark the edges of the layers and the van der Waals gap between them). **b**, Higher-resolution, and **c**, zoomed-in STEM images of the same sample. **d**, Energy dispersive spectroscopy (EDS) showing the elemental distribution of Nb, P, W, and S (combined), and of **e**, Nb, **f**, P, **g**, W, and **h**, S atoms (separately). The EDS measurement scan time was short to minimize electron-beam damage of the NbP/WS₂ stack and interface. This led to a lower-resolution EDS as a trade-off. **i**, Surface mapping with atomic force microscopy of ~3.5 nm NbP on bilayer WS₂ and nearby SiO₂ substrate, showing similar low surface roughness on both regions (~0.16 nm) (see **Supplementary Fig. 4**). Inset shows a cross-section schematic of the NbP covering steps of monolayer (1L) and bilayer (2L) WS₂. **j**, Raman spectra (532 nm laser, at room temperature) of bilayer WS₂ before (gray) and after (blue and red) being covered by NbP of two different thicknesses (~2 nm and ~3.5 nm), all showing similar E_g and A_{1g} peaks (normalized to the E_g peak intensity). The E_g and A_{1g} peaks correspond to in-plane and out-of-plane atomic vibrations, respectively.

Fig. 3c displays measured drain current vs. gate voltage (I_D vs V_{GS}) of bilayer WS₂ transistors, revealing >100× larger $|I_{D,max}|$ for our NbP-contact devices than our control Pd-contact devices. Similarly, our bilayer WS₂ devices with TaP contacts (another topological semimetal candidate) also show enhanced *p*-type current compared to control Pd contacts (**Supplementary Fig. S5a**). When probing

the positive V_{GS} range (**Supplementary Fig. S6**), Pd-contacted bilayer WS_2 devices also show stronger n -type behavior, similar to previous reports on ultrathin WS_2 using traditional metal contacts^{22,23}.

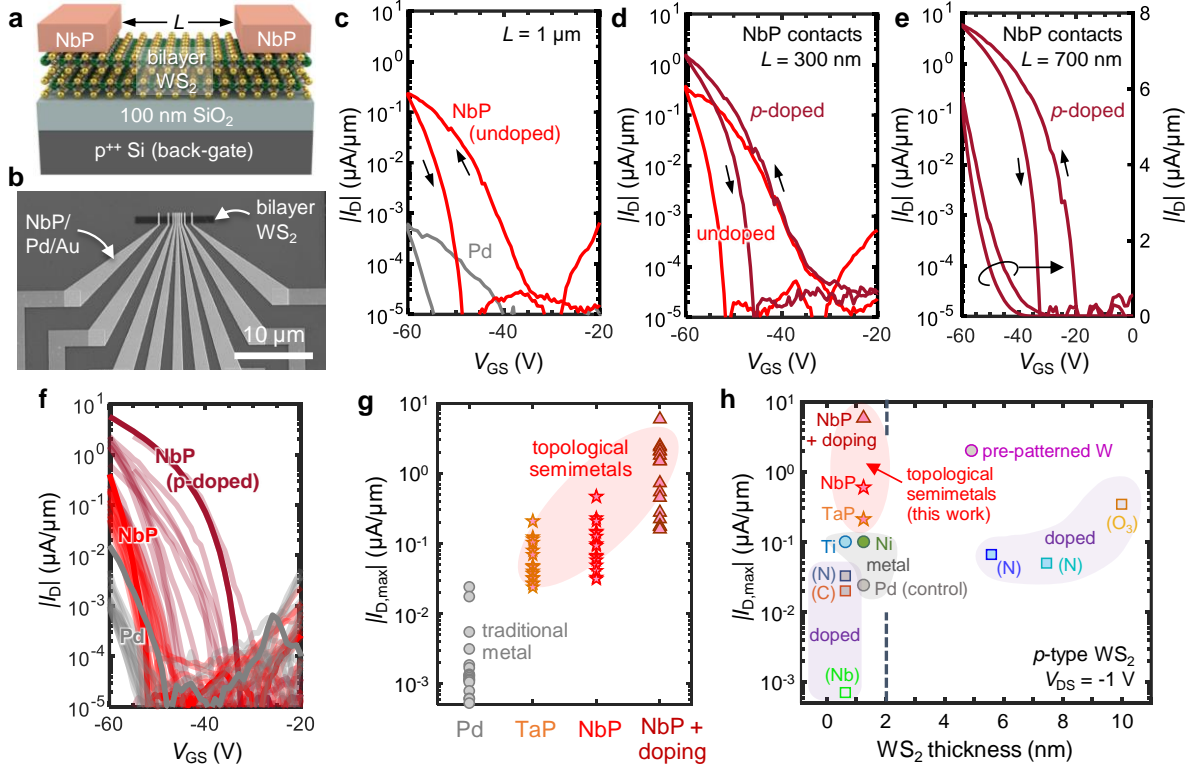


Figure 3 | Bilayer WS_2 transistors with NbP and TaP semimetal contacts. **a**, Schematic of a back-gated bilayer WS_2 transistor, not to scale. **b**, Top-view SEM image of fabricated devices with NbP contacts capped by Pd/Au. **c**, Measured I_D vs. V_{GS} at $V_{DS} = -1$ V for bilayer WS_2 transistors with NbP contacts (red) and Pd contacts (gray), at channel length $L = 1$ μm . Small arrows mark forward and backward sweeps²⁴, revealing similar hysteresis with both contact types. **d**, I_D vs. V_{GS} at $V_{DS} = -1$ V for a different bilayer WS_2 device ($L = 300$ nm) with NbP contacts before (red) and after (dark red) additional p -type doping, achieved by soaking the device in chloroform. **e**, I_D vs. V_{GS} at $V_{DS} = -1$ V showing maximum hole current of 5.8 $\mu\text{A}/\mu\text{m}$ in another bilayer WS_2 device ($L = 700$ nm) with NbP semimetal contacts and additional p -doping. I_D is shown on both linear and log scale axes. **f**, Measured I_D vs. V_{GS} at $V_{DS} = -1$ V for 15 bilayer devices (each) with Pd contacts (gray), NbP contacts (red), and NbP contacts with additional doping (dark red). Darker color lines represent the highest-current device of each kind. **g**, Maximum p -type current $|I_{D,max}|$ achieved at $V_{DS} = -1$ V of devices with various contacts, including Pd, TaP (another topological semimetal), and NbP (before and after additional doping); 15 devices (symbols) are shown for each type. **h**, Benchmarking maximum p -type current $|I_{D,max}|$ vs. WS_2 (channel) thickness at $V_{DS} = -1$ V with various contact materials and doping strategies^{25–32}, including NbP and TaP semimetals, and control Pd metal from this work. (Text labels in parenthesis next to the symbols represent the doping type used.) Our results with NbP semimetal contacts enable the highest hole currents to date (up to 5.8 $\mu\text{A}/\mu\text{m}$) achieved in bilayer WS_2 , $>50\times$ larger than previous reports with sub-2 nm channel thickness. All devices in panels **c–g** are between 1 and 2 μm wide, and the I_D reported is normalized ($\mu\text{A}/\mu\text{m}$) by the channel widths²⁴.

To further increase the p -type current of our NbP-contacted bilayer WS_2 devices we applied chloroform doping^{33,34} (see **Methods**). With this, we measured $|I_{D,max}|$ up to 5.8 $\mu\text{A}/\mu\text{m}$ at $V_{DS} = -1$ V, nearly an order of magnitude higher than before doping, as shown in **Fig. 3d–f** and **Supplementary Fig. S7a,b**. The chloroform-doped devices also show a positive shift of threshold voltage, another signature

of *p*-type doping. These doped WS₂ devices are surprisingly stable over time (up to 16 days), despite being simply stored in a nitrogen environment, uncapped (**Supplementary Fig. S7c,d**).

We summarize the maximum *p*-type current achieved from various bilayer WS₂ devices using different contacts in **Fig. 3g** (15 devices for each contact type). Despite the device-to-device variability, much of it inherent to academic nanofabrication, we note a clear trend of enhanced *p*-type conduction with our semimetal contacts (TaP and NbP) vs. conventional Pd contacts. With NbP contacts and doping, the *p*-type current is increased by two orders of magnitude vs. Pd contacts to bilayer WS₂.

We also note that the observed hysteresis remains a challenge in *p*-type TMDs on SiO₂³⁵ (compared to *n*-type MoS₂), and is often not reported. The hysteresis likely occurs due to the alignment of the TMD valence band with trap states in the SiO₂³⁶, due to interface adsorbates remaining from the TMD layer transfer process³⁷, and due to the imperfect nature of the as-grown materials today³⁸. These drawbacks are not fundamental, and are expected to be resolved as the quality of dielectrics, TMDs, and their interfaces improves. Nevertheless, fair device-to-device comparisons can be made when sufficient devices are measured and only the contacts are changed, as in **Fig. 3f,g**.

Using NbP and TaP semimetal contacts, we achieved the highest *p*-type currents to date in sub-2 nm thin WS₂ (**Fig. 3h**). Including doping, our devices reached ~5.8 μA/μm at $V_{DS} = -1$ V, over 50× higher than previous reports in this WS₂ thickness regime. In contrast, traditional metal contacts like Ti²⁷, Ni²⁸, or our control Pd show much suppressed *p*-type behavior on ultrathin WS₂. Thicker WS₂ (e.g., ~5 nm) grown from pre-patterned tungsten contacts does show *p*-type conduction³⁰; however, this thickness offers no electrostatic benefits over silicon in nanoscale transistors. **Fig. 3h** also displays additional data with traditional metal contacts to WS₂, where relatively low *p*-type currents were obtained after substitutional doping (using Nb²⁹, C²⁶, N^{25,31}) or charge-transfer doping (e.g., WO_x³²).

We note that the highest measured $|I_{D,max}|$ in our devices is limited by the largest $|V_{GS}|$ we can apply without compromising the back-gate dielectric integrity. In addition, the valence band of bilayer WS₂ is sufficiently ‘deep’ so as to render the threshold voltage quite negative here. This means that, even at our highest $|V_{GS}| = 60$ V, not all our devices are fully turned on, especially not the Pd-contacted ones (**Fig. 3f**). Nevertheless, we can estimate an upper bound of ~80 kΩ·μm for the *p*-type contact resistance of NbP to bilayer WS₂, as half the total resistance of the device with the highest current. Although better *p*-type contacts have been achieved with WSe₂ (which has a ‘shallower’ valence band)¹⁴, our estimated contact resistance to WS₂ is presently ~50× lower than any previous results with this 2D semiconductor at sub-2 nm thickness (see **Supplementary Fig. S8**).

To gain a deeper understanding of what enables the p -type behavior in NbP-contacted bilayer WS₂, we performed DFT simulations using Quantum ESPRESSO³⁹. We perform fixed-cell relaxations of the contact schematic shown in **Fig. 4a**, then extract the DOS and the hole Schottky barrier height $\phi_{B,p} = E_F - E_V$, as labeled on **Fig. 4b,c**. We estimate the density of metal-induced gap states (MIGS) by integrating the DOS across the band gap. The locations of WS₂ band edges are approximate, due to the presence of MIGS, and further simulation details are given in the **Methods** section.

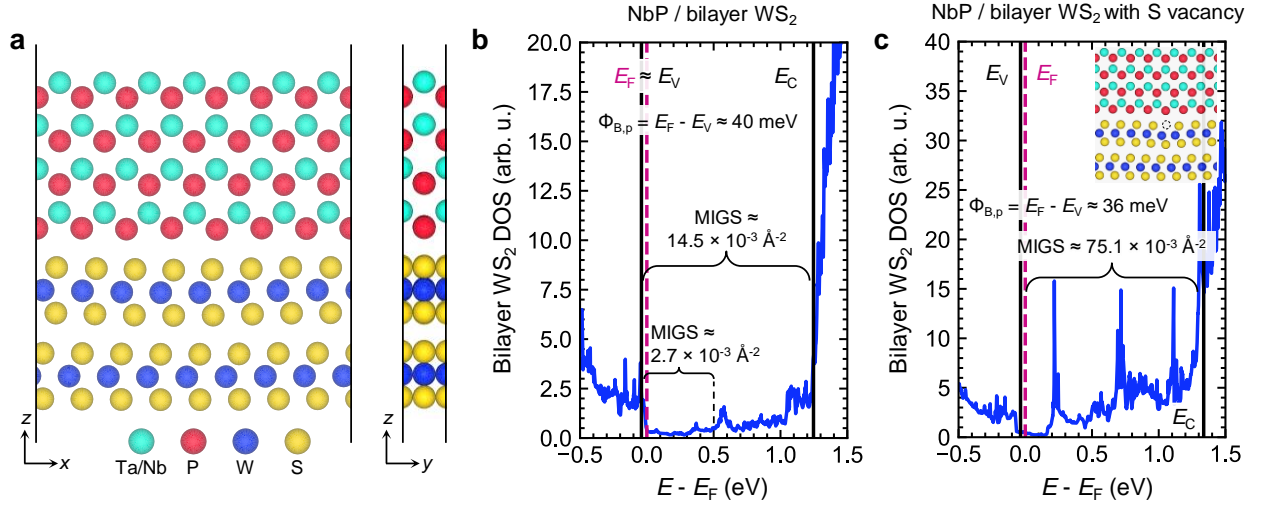


Figure 4 | Density Functional Theory (DFT) Simulations. **a**, Cross-section schematics of the DFT supercell for the semimetal contact (NbP or TaP) with bilayer WS₂. (Left) x - z cut and (right) y - z cut. **b**, Projected density of states (pDOS) contributions from bilayer WS₂ to the overall DOS of the NbP contact with bilayer WS₂. The hole Schottky barrier height is ≈ 0 meV. **c**, pDOS for the same contact but with one S vacancy (defect density of $\sim 1.4 \times 10^{14} \text{ cm}^{-2}$), displaying a small hole Schottky barrier height, ≈ 36 meV. The inset displays the supercell with the sulfur vacancy marked by a black dotted line. In panels **b-c**, the Fermi energy E_F is set to zero and marked with a dashed purple line; the valence band maximum E_V and conduction band minimum E_C are marked with solid black lines. Locations of band extrema are determined from projected band structures (see **Supplementary Section II**). MIGS densities are calculated by integrating the bilayer WS₂ pDOS across the denoted energy ranges.

In **Fig. 4b**, we estimate a small Schottky barrier ($\phi_{B,p} \approx 40$ meV) for the NbP contact with pristine bilayer WS₂, at first without defects. This behavior is comparable to the expected band alignment for an ideal scenario, without Fermi level pinning ($\phi_{B,p} \approx -100$ meV as detailed in **Supplementary Section D**). These results also suggest weak Fermi level pinning at the NbP/bilayer WS₂ interface because of the low MIGS densities formed, between $\sim 2.7 \times 10^{-3} \text{ \AA}^{-2}$ and $14.5 \times 10^{-3} \text{ \AA}^{-2}$, depending on the energy range of the DOS integral (the lower value being within 0.5 eV of E_V , where states are more likely to play a role in E_F pinning). We also simulate the bilayer WS₂ contact with TaP and find a hole barrier height of 14 meV, unlike the ideal pinning-free scenario of -200 meV (**Supplementary Fig. S9a**); however, experimentally we find TaP does not provide contacts as good as NbP to bilayer WS₂ (**Fig.**

3g,h), ostensibly due to greater damage during deposition. In contrast to these semimetals, our simulations for a conventional metal contact (W) on bilayer WS₂ reveal a large hole Schottky barrier ≈ 800 meV and large MIGS density ($\sim 176.3 \times 10^{-3} \text{ \AA}^{-2}$), as shown in **Supplementary Fig. S9b,c**. The estimated MIGS densities at our NbP/bilayer WS₂ contacts are also smaller than those of various conventional metal/2D semiconductor contacts from the literature^{14,40}.

We recall that the direct deposition of semimetals or conventional metals^{20,21} onto 2D semiconductors tends to create defects. To understand this, we performed additional DFT simulations (**Fig. 4c**) after introducing a sulfur (S) vacancy in the top WS₂ layer, corresponding to a high defect density of $\sim 1.4 \times 10^{14} \text{ cm}^{-2}$. Even in this case, we estimate a nearly unchanged $\phi_{B,p} \approx 36$ meV at our NbP contacts with bilayer WS₂, smaller than most metal-WS₂ systems^{14,40}. Together, the favorable band alignment between NbP and bilayer WS₂, with sufficiently small MIGS densities (which prevent strong Fermi level pinning) support the favorable *p*-type conduction observed in our experiments with NbP contacts. Our calculations suggest a larger, non-negligible hole Schottky barrier for NbP with *monolayer* WS₂ ($\phi_{B,p} \approx 550$ meV in **Supplementary Fig. S10**). This appears to occur due to the larger band gap and electron affinity (i.e., ‘deeper’ valence band) of monolayer WS₂ compared to bilayer WS₂.

In summary, we have introduced the topological semimetal NbP for improved *p*-type contacts to thin, bilayer WS₂. Together with doping, such NbP-contacted WS₂ transistors reach $5.8 \mu\text{A}/\mu\text{m}$ hole current (at $V_{DS} = -1$ V), over $50\times$ larger than previous *p*-type WS₂ devices with sub-2 nm thickness. The improved *p*-type performance is enabled by the simultaneously large work function and low density of states of the semimetal contacts, leading to small hole barrier heights. Notably, these contacts are deposited by sputtering at room temperature, a back-end-of-line compatible approach. These results provide physical insight into contact formation to the valence band of 2D semiconductors and demonstrate a possible route towards their incorporation into future CMOS nanoelectronics.

Acknowledgements. A.I.K. thanks James McVittie and Carsen Kline for their support and discussions about material deposition. Authors thank Ning Yang for useful discussions on the density functional theory simulation. Authors also thank Taehoon Cheon from Daegu Gyeongbuk Institute of Science and Technology (DGIST) for supporting TEM characterization. L.H. and E.P. acknowledge partial support from the SUPREME JUMP 2.0 center, a Semiconductor Research Corporation and DARPA program. R.K.A.B acknowledges support from the Stanford Graduate Fellowship and NSERC PGS-D Fellowship. M.H. acknowledges partial support from the US Department of Defense through the Grad-

uate Fellowship in STEM Diversity Program. Part of this work was performed at the Stanford Nanofabrication Facility (SNF) and Stanford Nano Shared Facilities (SNSF), supported by the National Science Foundation award EECS-2026822. Another part of this work was supported by the National Research Foundation of Korea (NRF) grant funded by the Korean government (MSIT) (RS-2024-00357895).

Author contributions. A.I.K. conceived the idea together with L.H. L.H. and A.I.K designed the experiments. A.I.K. formulated the semimetal contact deposition process and optimized it with input from L.H. WS₂ growth was performed by Z.Z. and L.H. L.H. performed AFM and Raman characterization, fabricated the devices, and performed electrical measurements with input from A.M. M.H. and L.H. performed and prepared samples for KPFM measurements. TEM and EDS characterization and analysis were performed by H-M.K. I-K.O. and A-R.C with input from A.I.K. R.K.A.B performed the simulations and relevant analysis with input from A.I.K and L.H. L.H., A.I.K., and R.K.A.B. wrote the manuscript together with E.P and A.M. All authors edited the manuscript.

Competing interests. A.I.K, L.H., R.K.A.B, E.P and A.M. are listed as co-inventors on a US patent provisional application (patent application number 63/572048) filed by The Board of Trustees of The Leland Stanford Junior University.

Data and materials availability: All data needed to evaluate the conclusions in this paper are present in the paper or the supplementary materials.

Supplementary Information

Available upon request from the authors and/or when the manuscript is formally published.

References:

1. de Vries, A. The growing energy footprint of artificial intelligence. *Joule* **7**, 2191–2194 (2023).
2. Srimani, T. *et al.* N3XT 3D Technology Foundations and Their Lab-to-Fab: Omni 3D Logic, Logic+Memory Ultra-Dense 3D, 3D Thermal Scaffolding. in *2023 International Electron Devices Meeting (IEDM)* 1–4 (IEEE, 2023). doi:10.1109/IEDM45741.2023.10413794.
3. Schmitz, J. Low temperature thin films for next-generation microelectronics. *Surf. Coatings Technol.* **343**, 83–88 (2018).
4. Fenouillet-Beranger, C. *et al.* A Review of Low Temperature Process Modules Leading Up to the First (≤ 500 °C) Planar FDSOI CMOS Devices for 3-D Sequential Integration. *IEEE Trans. Electron Devices* **68**, 3142–3148 (2021).
5. Wanlass, F. & Sah, C. Nanowatt logic using field-effect metal-oxide semiconductor triodes. in *1963 IEEE International Solid-State Circuits Conference* 32–33 (IEEE, 1963). doi:10.1109/ISSCC.1963.1157450.
6. Huang, C.-Y. *et al.* 3-D Self-aligned Stacked NMOS-on-PMOS Nanoribbon Transistors for Continued Moore’s Law Scaling. in *2020 International Electron Devices Meeting (IEDM)* 20.6.1-20.6.4 (IEEE, 2020). doi:10.1109/IEDM13553.2020.9372066.
7. Chung, Y.-Y. *et al.* First Demonstration of GAA Monolayer-MoS₂ Nanosheet nFET with 410 μ A/ μ m I_D 1V V_D at 40nm gate length. in *2022 International Electron Devices Meeting (IEDM)*

- 34.5.1-34.5.4 (IEEE, 2022). doi:10.1109/IEDM45625.2022.10019563.
8. Das, S. *et al.* Transistors based on two-dimensional materials for future integrated circuits. *Nat. Electron.* **4**, 786–799 (2021).
 9. Su, S.-K. *et al.* Layered Semiconducting 2D Materials for Future Transistor Applications. *Small Struct.* **2**, 2000103 (2021).
 10. Zhu, J. *et al.* Low-thermal-budget synthesis of monolayer molybdenum disulfide for silicon back-end-of-line integration on a 200 mm platform. *Nat. Nanotechnol.* **18**, 456–463 (2023).
 11. Tang, A. *et al.* Toward Low-Temperature Solid-Source Synthesis of Monolayer MoS₂. *ACS Appl. Mater. Interfaces* **13**, 41866–41874 (2021).
 12. Li, D., Wang, X., Mo, X., Tse, E. C. M. & Cui, X. Electronic gap characterization at mesoscopic scale via scanning probe microscopy under ambient conditions. *Nat. Commun.* **13**, 4648 (2022).
 13. Shen, P.-C. *et al.* Ultralow contact resistance between semimetal and monolayer semiconductors. *Nature* **593**, 211–217 (2021).
 14. Yang, N. *et al.* Ab Initio Computational Screening and Performance Assessment of van der Waals and Semimetallic Contacts to Monolayer WSe₂ P-Type Field-Effect Transistors. *IEEE Trans. Electron Devices* **70**, 2090–2097 (2023).
 15. Shekhar, C. *et al.* Extremely large magnetoresistance and ultrahigh mobility in the topological Weyl semimetal candidate NbP. *Nat. Phys.* **11**, 645–649 (2015).
 16. Khan, A. I. *et al.* Exceptional Reduction of Electrical Resistivity in Ultrathin Non-Crystalline NbP Semimetal. *arXiv Preprint*, arXiv: 2409.17337 (2024). <https://arxiv.org/abs/2409.17337>
 17. Corbae, P. *et al.* Observation of spin-momentum locked surface states in amorphous Bi₂Se₃. *Nat. Mater.* **22**, 200–206 (2023).
 18. Zhang, Z. *et al.* Chemically Tailored Growth of 2D Semiconductors via Hybrid Metal-Organic Chemical Vapor Deposition. *arXiv Prepr.* 2403.03482 (2024).
 19. Gong, C. *et al.* Metal Contacts on Physical Vapor Deposited Monolayer MoS₂. *ACS Nano* **7**, 11350–11357 (2013).
 20. Schauble, K. *et al.* Uncovering the effects of metal contacts on monolayer MoS₂. *ACS Nano* **14**, 14798–14808 (2020).
 21. Wu, R. J. *et al.* Visualizing the metal- MoS₂ contacts in two-dimensional field-effect transistors with atomic resolution. *Phys. Rev. Mater.* **3**, 111001 (2019).
 22. Wan, Y. *et al.* Low-defect-density WS₂ by hydroxide vapor phase deposition. *Nat. Commun.* **13**, 4149 (2022).
 23. Sun, Z. *et al.* Statistical Assessment of High-Performance Scaled Double-Gate Transistors from Monolayer WS₂. *ACS Nano* **16**, 14942–14950 (2022).
 24. Cheng, Z. *et al.* How to report and benchmark emerging field-effect transistors. *Nat. Electron.* **5**, 416–423 (2022).
 25. Tang, B. *et al.* Direct n- to p-Type Channel Conversion in Monolayer/Few-Layer WS₂ Field-Effect Transistors by Atomic Nitrogen Treatment. *ACS Nano* **12**, 2506–2513 (2018).
 26. Zhang, F. *et al.* Carbon doping of WS₂ monolayers: Bandgap reduction and p-type doping transport. *Sci. Adv.* **5**, 5003–5027 (2019).
 27. Asselberghs, I. *et al.* Wafer-scale integration of double gated WS₂-transistors in 300mm Si CMOS fab. in *2020 IEEE International Electron Devices Meeting (IEDM)* 40.2.1-40.2.4 (IEEE, 2020). doi:10.1109/IEDM13553.2020.9371926.
 28. Lin, D. *et al.* Dual gate synthetic WS₂ MOSFETs with 120 μ S/ μ m Gm 2.7 μ F/cm² capacitance and ambipolar channel. in *2020 IEEE International Electron Devices Meeting (IEDM)* 3.6.1-3.6.4 (IEEE, 2020). doi:10.1109/IEDM13553.2020.9372055.
 29. Zhang, P. *et al.* Transition-Metal Substitution-Induced Lattice Strain and Electrical Polarity Reversal in Monolayer WS₂. *ACS Appl. Mater. Interfaces* **12**, 18650–18659 (2020).
 30. Chung, Y.-Y. *et al.* Demonstration of 40-nm Channel Length Top-Gate p-MOSFET of WS₂ Channel Directly Grown on SiO_x/Si Substrates Using Area-Selective CVD Technology. *IEEE Trans. Electron Devices* **66**, 5381–5386 (2019).

31. Cao, Q. *et al.* Realizing Stable p-Type Transporting in Two-Dimensional WS₂ Films. *ACS Appl. Mater. Interfaces* **9**, 18215–18221 (2017).
32. Kato, R. *et al.* p-Type Conversion of WS₂ and WSe₂ by Position-Selective Oxidation Doping and Its Application in Top Gate Transistors. *ACS Appl. Mater. Interfaces* **15**, 26977–26984 (2023).
33. Choi, J., Zhang, H., Du, H. & Choi, J. H. Understanding Solvent Effects on the Properties of Two-Dimensional Transition Metal Dichalcogenides. *ACS Appl. Mater. Interfaces* **8**, 8864–8869 (2016).
34. Kim, H. H. *et al.* Substrate-induced solvent intercalation for stable graphene doping. *ACS Nano* **7**, 1155–1162 (2013).
35. Ho, P. H. *et al.* High-Performance WSe₂ Top-Gate Devices with Strong Spacer Doping. *Nano Lett.* **23**, 10236–10242 (2023).
36. Knobloch, T. *et al.* Improving stability in two-dimensional transistors with amorphous gate oxides by Fermi-level tuning. *Nat. Electron.* **5**, 356–366 (2022).
37. Tilmann, R. *et al.* Identification of Ubiquitously Present Polymeric Adlayers on 2D Transition Metal Dichalcogenides. *ACS Nano* **17**, 10617–10627 (2023).
38. Ho, P.-H. *et al.* Hysteresis-Free Contact Doping for High-Performance Two-Dimensional Electronics. *ACS Nano* **17**, 2653–2660 (2023).
39. Giannozzi, P. *et al.* Quantum ESPRESSO toward the exascale. *J. Chem. Phys.* **152**, 154105 (2020).
40. Tang, H. *et al.* Schottky Contact in Monolayer WS₂ Field-Effect Transistors. *Adv. Theory Simulations* **2**, 1900001 (2019).
41. Dal Corso, A. Pseudopotentials periodic table: From H to Pu. *Comput. Mater. Sci.* **95**, 337–350 (2014).
42. Grimme, S. Semiempirical GGA-type density functional constructed with a long-range dispersion correction. *J. Comput. Chem.* **27**, 1787–1799 (2006).
43. Sohler, T., Calandra, M. & Mauri, F. Density functional perturbation theory for gated two-dimensional heterostructures: Theoretical developments and application to flexural phonons in graphene. *Phys. Rev. B* **96**, 075448 (2017).
44. Kawamura, M., Gohda, Y. & Tsuneyuki, S. Improved tetrahedron method for the Brillouin-zone integration applicable to response functions. *Phys. Rev. B* **89**, 094515 (2014).